REVIEW

National Science Review
6: 642–652, 2019
doi: 10.1093/nsr/nwz055
Advance access publication 2 May 2019

MATERIALS SCIENCE

Special Topic: Multiferroic Physics and Materials

Lattice and spin dynamics in multiferroic $BiFeO_3$ and $RMnO_3$

Yan Song, Ben Xu* and Ce-Wen Nan

ABSTRACT

The multiferroic materials $BiFeO_3$ and $RMnO_3$ exhibit coexisting magnetic order and ferroelectricity, and provide exciting platforms for new physics and potentially novel devices, where intriguing interplay between phonons and magnons exists. In this review, we paint a complete picture of bulk $BiFeO_3$ together with orthorhombic and hexagonal $RMnO_3$ (R includes rare-earth elements and yttrium) by summarizing the dynamics of spin and lattice and their magnetoelectric coupling, as well as the methods of controlling these characteristics under non-equilibrium conditions, from experimental and simulation perspectives.

Keywords: multiferroics, phonon, magnon

INTRODUCTION

The advancement beyond complementary metal-oxide-semiconductor devices demands materials with strong logic state stability and high switching efficiency [1,2]. Multiferroic materials are intrinsically promising candidates in this regard because their low energy dissipation in switching and high energy efficiency form a barrier to stabilize the order parameter [2]. However, it is still challenging to overcome the precession timescale limitation and switch the multiferroic antiferromagnetic (AFM) state with a high stability of $100k_BT$ locally on the nanoscale. The recently demonstrated possibility of direct pumping of spin excitations in AFM materials with the help of a freely propagating terahertz (THz) wave suggests that such waves are strongly coupled to the excitations in the medium and provide a useful pathway for manipulating the material structure and properties to overcome the abovementioned limitation. In these processes, the coupling between the lattice and spin excitations is essential; however, this topic remains highly underrated and not sufficiently understood.

The collective lattice and spin excitations are addressed as quantized waves called phonons and magnons. Both phonons and magnons obey boson behavior and therefore follow Bose–Einstein statistics [3]. These quasiparticles can be completely described by their dispersion relations between energy (frequency) and wave vector, which is important for understanding atomic bonding, to determine the underlying interactions governing the spin dynamics and obtain detailed information about complex spin structures (Fig. 1) [4]. Strong anharmonicity exists in multiferroics and allows higher-order zone-center magnons to become dipole active, i.e. to become other quantized excitations unique in multiferroics as electromagnons [5,6].

$BiFeO_3$ (BFO) and $RMnO_3$ (R includes rare-earth elements and yttrium) are the two most widely studied multiferroics. BFO and hexagonal (h)-$RMnO_3$ are type-I multiferroics whose ferroelectric (FE) transition temperatures are well above their magnetic ones. Meanwhile, orthorhombic (o)-$RMnO_3$ (e.g. $TbMnO_3$, $DyMnO_3$ and $(Tb, Gd)MnO_3$) is a type-II multiferroic with strong magnetoelectric (ME) coupling, and the ordered phases occur at very low temperatures. It is worth mentioning that not all o-$RMnO_3$ are multiferroics, e.g. manganites with R = Nd, Sm, Eu, Ho are not multiferroics. The remainder of this review is divided into two main parts: firstly, we focus on experimental investigations as well as the manipulation of phonons, magnons, electromagnons,

School of Materials Science and Engineering, and State Key Laboratory of New Ceramics and Fine Processing, Tsinghua University, Beijing 100084, China

*Corresponding author. E-mail: xuben@mail.tsinghua.edu.cn

Received 11 January 2019; **Revised** 3 April 2019; **Accepted** 10 April 2019

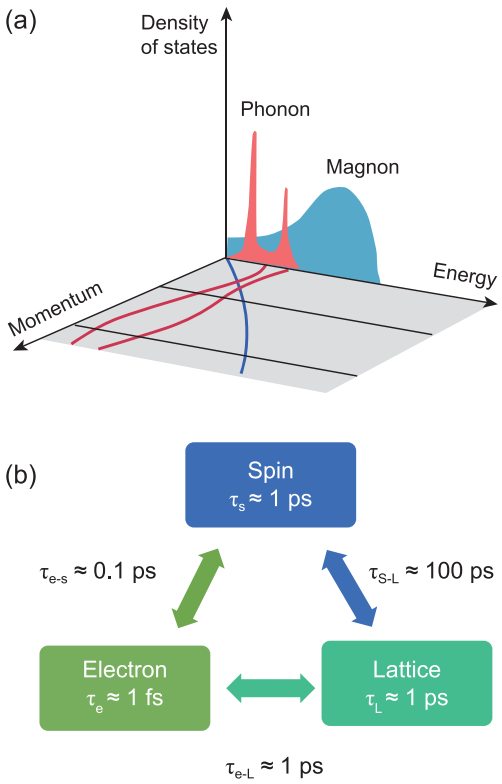

Figure 1. (a) Energy–momentum relation of phonons and magnons in complex solids. (b) Schematic of the three subsystems with their characteristic relaxation times and coupling parameters.

and the coupling between them in BFO and RMnO$_3$; then, we address the simulations and prediction schemes used to demonstrate and manipulate the dynamics of phonons and magnons. Finally, we summarize the conclusions.

EXPERIMENTS

At present, experimental measurements of phonons and magnons are performed using two main types of methods: inelastic neutron scattering (INS) and optical techniques, where Raman, infrared (IR), and THz spectroscopy are most commonly used; these have different selection rules and spectral weights [7]. INS could be used to measure the dispersion relations in full momentum space, whereas optical means are restricted to near the Brillouin zone (BZ) center. However, the energy resolution of INS in the low-energy region is rather poor, while THz spectroscopy exhibits superiority in this region. INS measures phonon and magnon spectra in the whole BZ including electromagnons, but hybrid excitations can only be determined by IR or THz spectra based on full polarization analysis, observation of directional dichroism or transfer of oscillator strength of some polar phonon to spin excitation [8,9].

Phonons

The vibrational spectra of BFO [8,10–17], *o*-RMnO$_3$ [18], and *h*-RMnO$_3$ [7,19–23] have been well characterized. All of them converge to a common phonon picture reflecting the symmetry of the crystals. The symmetry of BFO is rhombohedral R3c [11], and P6$_3$cm and P6$_3$/mmc for the FE and paraelectric states of *h*-YMnO$_3$ [7]. Note that usually fewer phonons are experimentally observed than that are allowed by symmetry, because some of the modes are overlapping or have low intensities. The phonon symmetry needs to be correctly assigned using polarized Raman techniques [12,14,24] and infrared spectroscopy [8,17,18,22]. This symmetry information of phonons is crucial for understanding the nature of phase transitions and identifying connections between physical properties and atomic motions [25–27].

As the temperature increases, the energy of particular phonon modes decreases because of bond softening [10,11], and some of them disappear due to the crystal structure change above FE transition. Moreover, the phonon density of states measured by INS shows broadening of the entire phonon spectrum, indicating strong anharmonicity due to phonon–phonon interactions [28]. Hybridization or coupling also occurs between different branches [29].

Magnons

In type-I multiferroics, since the FE transition takes place at higher temperatures than the magnetic ordering, unperturbed magnon (phonon) dispersion can be measured below (above) T_N. The non-spin-flip data capture the phonon signal, while the spin-flip signal is purely magnetic.

The zone-center frequencies of magnons are normally below those of phonons, with high-energy spin dynamics for super-exchange interaction including the nearest neighbor (NN) and next-nearest neighbor (NNN) exchanges, and low-energy spin dynamics for inter-layer coupling and single-ion anisotropy (SIA) [6], where discrepancies still exist between the simulation and dispersion curves obtained experimentally [30]. The ratio between the NN and NNN exchanges determines the local AFM order, and the Dzyaloshinskii–Moriya interaction (DMI) stabilizes a long-period spin cycloid in BFO.

In BFO, spin cycloids excite two categories of magnons corresponding to spin-wave excitations:

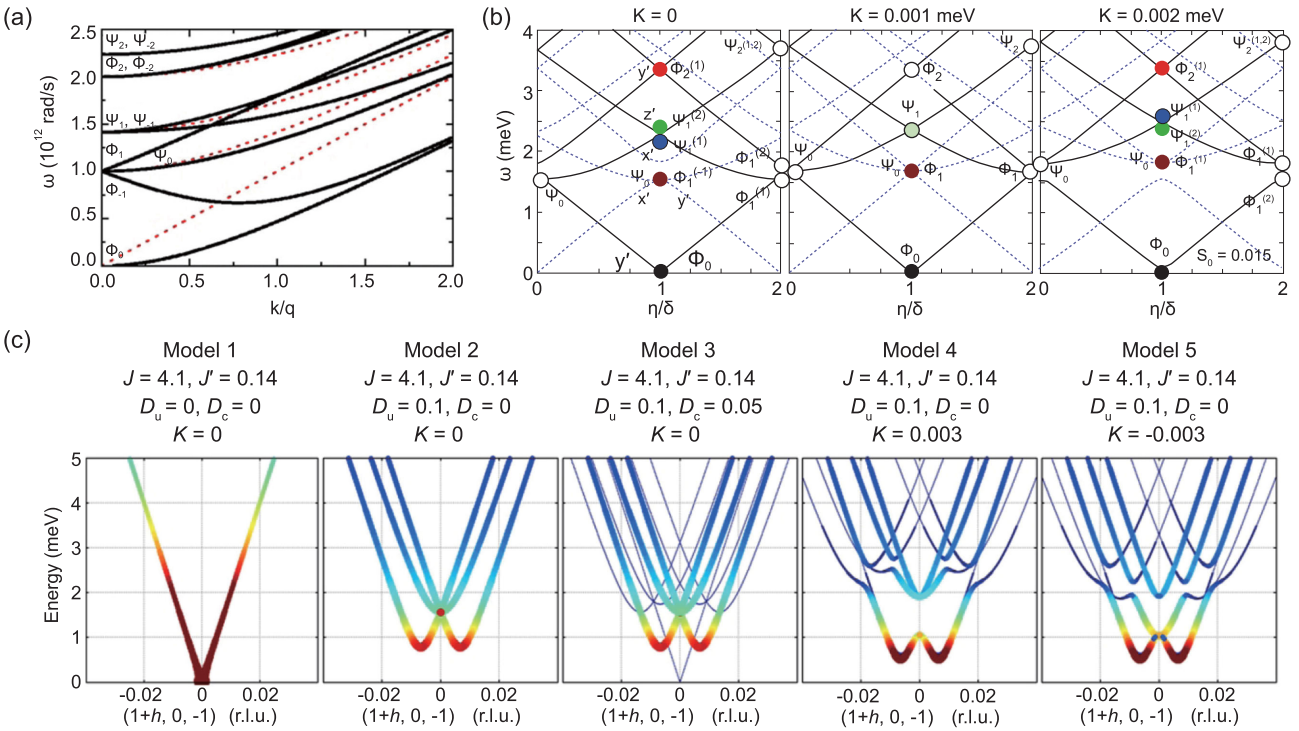

Figure 2. (a) Theoretical result of the magnon spectrum for a cycloid without the anisotropy term. The perpendicular component to the cycloid plane and parallel component along the polarization direction are depicted by the solid and dashed lines, respectively. The Φ_n (cyclon) and Ψ_n (extra-cyclon) are the in-plane and out-of-plane modes, respectively. (b) Magnon modes calculated by the full spin Hamiltonian. All possible excitations are showed by dashed lines. (c) Calculated magnon dispersion along $[h\ 0\ 0]_{hex}$ near $(1, 0, -1)_{hex}$ for several models described in the text [4]. Copyright 2019, IOP Publishing.

cyclons (denoted Φ, in the cycloid plane) and extra-cyclons (or spin-flip, denoted Ψ, out of the cycloid plane), which can be demonstrated using Raman spectroscopy [6], THz spectroscopy [5,8,31,32] and millimeter-wave and IR spectroscopy [15]. The peak locations of the Φ modes are equally spaced starting at zero frequency, while those in the Ψ sequence are not regularly spaced at low frequencies, in agreement with the theoretical prediction [33]. Different DMIs and SIAs can only introduce significant changes at the zone center at lower energies (shown in Fig. 2) [4]. In $TbMnO_3$, three modes exist corresponding to the rotation of both the spin plane and polarization direction about the *z* axis; rotation of the spin plane about the *x* axis, which is not coupled to the polarization; and the sliding mode, i.e. phason, of the spiral [34], and have been observed in INS [35] and THz studies [36–41]. Moreover, multiple excitation modes such as two-magnon modes have been observed in IR reflectivity spectra of $TbMnO_3$ [9].

In *h*-$RMnO_3$, such as $YMnO_3$, the spins on Mn^{3+} ions are ordered antiferromagnetically and frustrated strongly on triangles in the *ab* plane with a 120° angle. Magnons were investigated using IR, THz and Raman spectroscopies [7,42]. Excitation at the zone boundary in the *ab* plane and linear field-induced magnon dispersion splitting close to the zone center [43] suggest a possible 3D magnetic ground state of the system. However, discrepancies still exist between INS dispersion curves and theoretical calculations of the exchange parameter ratio J_{NN}/J_{NNN}, which implies that the standard interpretation of magnon spectra needs to be revised and that magnon–phonon and magnon–magnon interactions need to be included.

When increasing the temperature or magnetic field, softening and broadening occur in the spin-wave spectrum [28], which reflects the frustrating NNN interactions, weakened NN interactions, and strong anharmonicity of the magnon–magnon and magnon–phonon interactions. Moreover, non-monotonic behavior of the INS scattering intensity has been observed with increasing temperature [44]. Broadening of the magnon spectrum and excitation splitting have been found [8,45], although they require further study [35].

Phonon–magnon coupling and electromagnons

Generally, lattice and spin coupling manifest themselves as anomalous temperature dependence of the peak position deviating from standard

anharmonicity-related phonon decay and anomalous hardening below T_N [10,23,46]. When the phonon–magnon coupling becomes sufficiently strong, a complex magnetic phase can be introduced; e.g. a longitudinal spin-density wave and spiral phase can exist at different temperatures in $TbMnO_3$ [9]. Magnon–phonon coupling is so strong that it governs the polarization dependence of magnon absorption in BFO [47]. Most importantly, the transverse acoustic phonons measured at the zone boundary clearly broaden in energy when T_N is approached from below, indicating that the acoustic phonon modes and magnetic order are coupled in this multiferroic material [29].

A quasiparticle called an electromagnon (EM) [48–51] can be excited and is a hybrid of magnon- and phonon-like modes, which can be excited by the electric and magnetic fields of a photon, respectively. The activation of these excitations can stem from either DM interaction [33,52–55], or exchange striction [37,56,57]. In addition to mixing the modes, the ME coupling shifts the frequencies with respect to the bare magnon or phonon frequencies. However, these energy shifts are small [33,52] in BFO, so the magnetic resonances and electromagnons are coincident within the experimental resolution. Depending on the magnetic modulation and anharmonicity of the material, EM with higher quantum number can appear, which can be attributed to Umklapp coupling between magnons and phonons [33,52] as well as non-zero SIA, where the latter can also split Ψ_n and Φ_n to $\Psi_{\pm n}$ and $\Phi_{\pm n}$ [6,45], as shown by THz spectroscopy [5] of BFO, *o*-$RMnO_3$ [9,38–40]. However, it is still under debate why optical phonons and electromagnons that are separated by such a large energy scale can experience direct coupling.

In *h*-$RMnO_3$, the FE and magnetic orderings are no longer concomitant since the electric polarization appears far above room temperature, while strong magnon–phonon coupling still exists. One of the consequences is that extra hardening deviation occurs below T_N for several phonon branches [20,22,23,46]. At the same time, strong deviations from linear spin-wave theory excluding magnon–phonon coupling have been observed in magnon dispersion curves [41]. Consequently, the lower mode at the BZ boundary moves downwards in energy and an additional mode at high energy appears in the phonon spectrum of *h*-$RMnO_3$. Moreover, avoided crossing (anti-crossing) at the zone boundary in polarized INS was revealed and exhibited mixed magnon–phonon characteristics [7,19,43,58]. Furthermore, spontaneous magnon decay, i.e. finite magnon lifetime, occurs because of the anharmonic higher-order terms caused by non-collinear spin structures [41].

Manipulation of phonons and magnons

Magnetic states can be manipulated either by switching the helicity of AFM-order spin cycloids in $TbMnO_3$ using a continuous-wave laser beam with an energy of 2.3 eV [59] or by tuning the motion of the magnetization vector to follow an arbitrarily designed direction and amplitude of polarization in NiO [60]. The latter method is performed by applying two linearly polarized laser pulses with a properly tuned azimuthal angle ψ and time delay τ [60]. A similar idea was later implemented in AFM three-sublattice ordering of the magnetic Mn^{3+} moments in hexagonal $YMnO_3$, where full 3D magnetization control was realized by a pair of time-delayed polarization-twisted femtosecond laser pulses [61]; thereby, it is possible to store multiple pieces of information.

SIMULATIONS

The following section will concentrate on theories and simulation techniques used to identify the magnetic interactions in multiferroic materials; to demonstrate the dispersion curves of phonons, magnons, and electromagnons; and lastly to manipulate the magnetic states based on the strong nonlinear phonon–magnon coupling.

Hamiltonian for multiferroic systems

The total Hamiltonian for multiferroic systems has been thoroughly reviewed in the previous literature [62] and can be expressed in several terms as $\mathcal{H}_{exch} + \mathcal{H}_{DM} + \mathcal{H}_{SIA}$, with the NN exchange J_{ij}, NNN exchange J'_{ij}, DMI D_{ij}, and SIA K_{SIA}. The exchange interaction $\mathcal{H}_{exch}$ can be expressed as

$$\mathcal{H}_{exch} = \sum_{r,i,j} J^*_{ij} S_i \cdot S_j = \sum_{r,NN} J_{ij} S_i \cdot S_{NN} + \sum_{r,NNN} J'_{ij} S_i \cdot S_{NNN}. \quad (1)$$

If $J_{ij} > 0$, the exchange interaction favors the AFM state, while, if $J_{ij} < 0$, it favors the ferromagnetic state. The DMI term $\mathcal{H}_{DM}$ contributes to the cycloid structure of spins and arises from the interplay between broken inversion symmetry and spin–orbit coupling [63,64], where

$$\mathcal{H}_{DM} = -\sum_{r,i,j} D_{ij} \cdot (S_i \times S_j). \quad (2)$$

The DMI favors perpendicular spin alignment, and the strength is proportional to the rotation angle of the oxygen octahedral. The SIA Hamiltonian is

$$\mathcal{H}_{\mathrm{SIA}} = -\mathcal{K}\sum_{r}(S_r\cdot\hat{c})^2 \tag{3}$$

For the uniaxial case, $\mathcal{K}>0$ corresponds to the easy axis and $\mathcal{K}<0$ to the easy plane. SIA comes mainly from anisotropic deformation of the structure as well as the competing FE and antiferrodistortive (AFD) distortions.

The above terms of the Hamiltonian dominate the magnetic behavior of BFO and *h*-$R\mathrm{MnO_3}$, although the DMI can be more specified in different directions. However, for *o*-$R\mathrm{MnO_3}$, the above Hamiltonians cannot precisely describe the complex phase diagram of magnetic states, such as the existence of E-AFM states. The Ising mode [65], two-orbital double-exchange model [66,67], and bond alternation model of FM exchange [68] were proposed, before higher-order coupling terms such as a biquadratic term $\mathcal{H}_{\mathrm{biq}}$ [69] and four-spin ring exchange term $\mathcal{H}_{\mathrm{4sp}}$ [70] were included to predict magnetic structures and important features of spin-wave spectra that cannot be obtained from the Heisenberg Hamiltonian [71–73]:

$$\mathcal{H}_{\mathrm{biq}} = -\sum_{i,j}B_{ij}(S_i\cdot S_j)^2 \tag{4}$$

$$\mathcal{H}_{\mathrm{4sp}} = \sum_{i,j,k,l}g_{ijkl}\big[(S_i\cdot S_j)(S_k\cdot S_j)+(S_i\cdot S_l)\times(S_j\cdot S_k)-(S_i\cdot S_k)(S_j\cdot S_l)\big]. \tag{5}$$

Higher-order exchange couplings can be obtained from the consecutive hopping of electrons between a series of four NN spins and have been invoked to describe the detailed energetics of orthorhombic $\mathrm{TbMnO_3}$, as in [69,74].

The four-spin ring Hamiltonian fits the energy of *o*-$R\mathrm{MnO_3}$ from DFT [69] and certain features in neutron diffraction patterns [75,76]. Moreover, it not only explains the unexpected polarization direction [76], but also solves the discrepancy between the predicted and observed orders of the electric polarization magnitude of E-AFM-ordered $\mathrm{TbMnO_3}$ [74,77–79].

Determination of exchange parameters

For precise evaluation of the above Hamiltonian, it is important to identify the coupling constants accurately [80], which can be done by using first-principles methods to calculate the total energy of four carefully designed collinear spin configurations. J_{ij}, D_{ij}, K_{SIA}, and their derivatives can then be obtained by extracting the linear combination of the energies $\mathcal{H}_1$, $\mathcal{H}_2$, $\mathcal{H}_3$, $\mathcal{H}_4$ of these four different configurations (Eq. (7)), where the forces can be obtained directly from many standardized DFT schemes as Hellmann–Feynman forces [81]. The total energy of the system with collinear spin alignment is calculated when spin states at two sites *i* and *j* within the given unit cell are modified, with the magnetism of the system fully described by the Heisenberg Hamiltonian

$$\mathcal{H}_{\mathrm{spin}} = J_{ij}\,S_i\cdot S_j + S_i\cdot Q_i + S_j\cdot P_j + \mathcal{H}_{\mathrm{other}}, \tag{6}$$

where $Q_i=\sum_{m\neq i,j}J_{im}S_m$, $P_j=\sum_{m\neq i,j}J_{jm}S_m$, and $\mathcal{H}_{\mathrm{other}}=\sum_{m\neq i,j}J_{mn}S_m\cdot S_n$,

$$J_{ij} = \frac{\mathcal{H}_1+\mathcal{H}_4-\mathcal{H}_2-\mathcal{H}_3}{4S^2}. \tag{7}$$

The derivative of J_{ij} with respect to the displacement $\xi_{k\alpha}$ can be found to be

$$\frac{\partial J_{ij}}{\partial\xi_{k\alpha}} = \frac{1}{4S^2}\left(\frac{\partial\mathcal{H}_1}{\partial\xi_{k\alpha}}+\frac{\partial\mathcal{H}_4}{\partial\xi_{k\alpha}}-\frac{\partial\mathcal{H}_2}{\partial\xi_{k\alpha}}-\frac{\partial\mathcal{H}_3}{\partial\xi_{k\alpha}}\right). \tag{8}$$

Regarding the system with its spin configuration in the non-collinear state, the calculation method remains the same in terms of still using four magnetic ions within a unit cell, while the total energy with respect to the rotation angle α away from the initial collinear state is fitted to the form of the Heisenberg model, where the exchange coupling constants J_{ab} and J_c can be extracted [82]. The problem of identifying coupling constants is essentially one of parameter fitting with certain numbers of equations and unknown constants. Based on this understanding, four spin ring coupling constants were evaluated for *o*-$R\mathrm{MnO_3}$ in an overdetermined system, where the energies of non-equivalent collinear magnetic orders were calculated for a number of states much greater than the number of constants [69]. An array of equations was solved by using the least mean squares method, and all of the abovementioned couplings were found.

Quasiparticle spectrum

The quantized excitations of the lattice or magnetic subsystem, namely, phonons and magnons, are completely described by their dispersion relation, which

is strongly dependent on the atomic bonding and magnetic coupling. Most multiferroic materials exhibit severe modification of the magnetic configuration alongside structural changes, indicating the possibility of strong phonon–magnon coupling.

Phonons

The starting point of phonon dispersion is correct evaluation of the strength of a particular distortion mode or force constant [83,84]. The former can be readily obtained using shell models [85,86], while the latter needs to be determined from the dynamical matrix of the system [87,88]. In these methods, the total energy is obtained by performing first-principles calculations, using different functionals such as the local density approximation (LDA), generalized gradient approximation (GGA), LDA+U, GGA-Wu–Cohen (WC), and Heyd–Scuseria–Ernzerhof functionals [26,89]. Note that although LDA can provide quantitively satisfying agreement with experimental results, some functionals can achieve much better agreement for particular branches, such as the B1-WC functional for the E modes in BFO [90].

Zone-center phonon frequencies of BFO obtained via the above methods fit well most of the peaks in absorption spectra obtained by either Raman or IR measurements [8,16,17,25,26,91,92]. Moreover, through e.g. detailed mode analysis, the transverse optic modes $A_1(TO_1)$ and $A_1(TO_2)$ were found to involve FE distortion and AFD rotation, respectively, in BFO, which was verified by Ginzburg–Landau calculations [33]. Furthermore, the effects of macroscopic electronic polarization can also be considered by including long-range Coulomb forces in DFT calculations [25,87]. Regarding RMnO$_3$, discrepancies still exist between the phonon spectra calculated using shell models and experimental measurements, which may be due to over-simplification in the shell model calculations [86]. Indeed, first-principles electronic structure calculations for YMnO$_3$ tend to yield higher phonon energies for the low-energy E_1 modes, compared with those obtained using the shell model [93].

Magnons

Magnon behavior has been reviewed for BFO [4] and h-RMnO$_3$ [94]. Generally speaking, the high- and low-energy parts of the magnon spectrum are dominated by super-exchange interactions such as J_{ij} and DMI/SIA, respectively, because DMI/SIA originates from spin–orbit coupling and is much weaker than the exchange interaction. Moreover, SIA will introduce anharmonic effects into a long cycloid or even destroy it if sufficiently strong.

Several methods of calculating magnon spectra to fit the peak positions in IR and Raman spectroscopy or the dispersion curves in full momentum space in INS have been proposed. In the first case, the stochastic Landau–Lifshitz–Gilbert (LLG) equation with fluctuation terms was considered, and peaks in magnetic susceptibility curves were shown to indicate magnons [27]. A similar method was implemented to obtain the magnon dispersion for BFO in the full BZ, starting from the Ginzburg–Landau free-energy expression [33] that includes the contributions of the AFM and FE order parameters L and P, respectively, as well as the interaction between them, as shown in the following equation:

$$\begin{aligned} F = & \frac{GL^4}{4} + \frac{AL^2}{2} + \frac{c\sum_i (\nabla L_i)^2}{2} \\ & - \alpha P \cdot [L(\nabla \cdot L) + L \times (\nabla \times L)] \\ & - P \cdot E + \frac{rM^2}{2} + \frac{aP_z^2}{2} + \frac{uP_z^4}{4} \\ & + \frac{a_\perp \left(P_x^2 + P_y^2\right)}{2} \end{aligned} \tag{9}$$

where $L = |M_1 - M_2|$ is a Néel vector describing the staggered sublattice magnetization; $M = |M_1 + M_2|$ is the total magnetization of the materials; and P_X, P_Y, and P_Z are the magnitudes of the FE polarization along the x, y, and z axes, respectively. Therefore, L can be determined from the linearized equations of motion for the FE and AFM order parameters obtained by the variational theorem. Basically, the simple spin waves can be determined from the fluctuations $\delta\mathbf{L}$, with the cyclon order parameter Φ and out-of-plane order parameter Ψ referring to the phase fluctuation of the cycloid ground state and spin fluctuation out of the cycloid plane (the xz plane), respectively:

$$\begin{aligned} \delta\mathbf{L} &= [\phi(\mathbf{r}), \psi(\mathbf{r}), \delta\mathbf{p}(\mathbf{r})] \\ &= \sum_n [\phi(\mathbf{r}), \psi(\mathbf{r}), \boldsymbol{p}_n]\, e^{inqx} e^{i\boldsymbol{k}\cdot\boldsymbol{r}}. \end{aligned} \tag{10}$$

Series of parabola-like dispersion curves of magnons were found, with anti-crossing between the optical phonon dispersion and magnon branches at finite k, and the frequency was dependent on $q = \alpha P_0/c$, where α and c are from the free-energy expression in Eq. (9), and P_0 is the polarization of an easy-axis FE with uniform polarization [33].

The other method of obtaining the full momentum space spectrum starts from the spin Hamiltonian mentioned in the previous section.

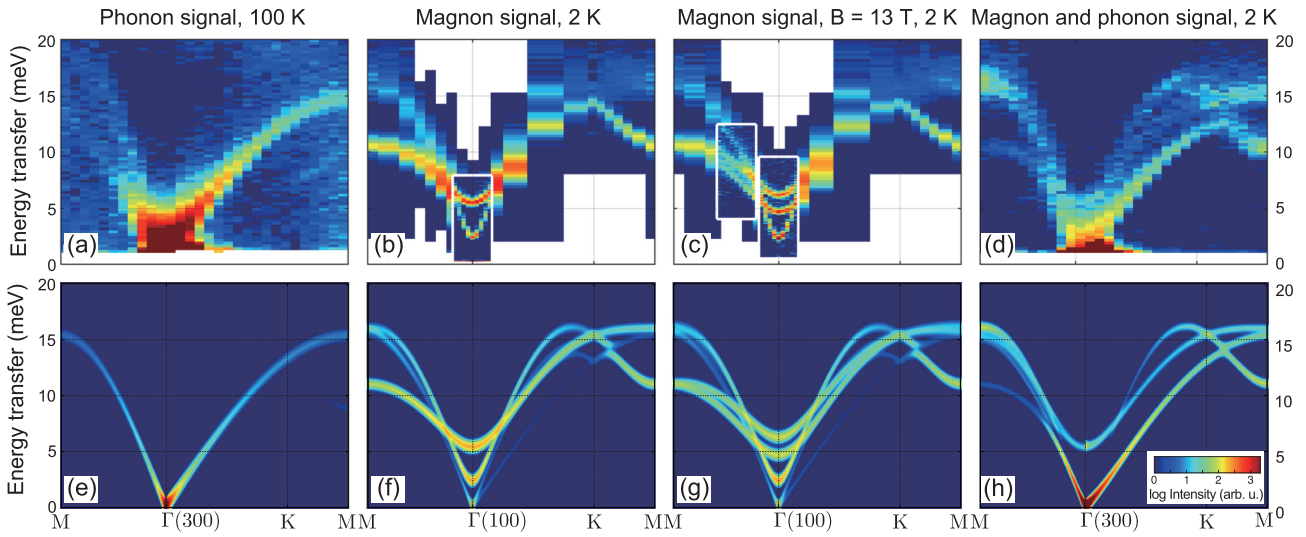

Figure 3. (a)–(d) Experimental magnon and phonon dispersions of *h*-$YMnO_3$. (e)–(h) Theoretical dispersions with intensity at the same *q* paths, temperatures, and applied magnetic fields [43]. Copyright 2019, American Physical Society.

A second quantization was implemented by using the Holstein–Primakoff boson operators [95], Bogoliubov transformation, and diagonalization. The Hamiltonian can consequently be expressed as

$$\mathcal{H}_{\text{exch}} = E_{\text{cl}} + S\sum_{k}\omega_k + \sum_{k} 2S\omega_k \gamma_k^{+}\gamma_k, \tag{11}$$

where E_{cl} is the classical ground-state energy, and the magnon energy can be found from $2S\omega_k$ [4,30,32,44,52,54,96]. To avoid needing a large unit cell to include the cycloid, local rotating coordinate systems were introduced both for BFO [4,52] and *o*-$RMnO_3$ [34,35].

In BFO, the magnon modes were separated into two groups, according to two effective components of DMI: cyclon (Φ) and extra-cyclon (Ψ) modes, as shown in Fig. 2 [33]. Φ modes are gapless, while Ψ modes are gapped due to the pinning of the cycloid plane. Once the excitation spectrum has been obtained precisely, the Hamiltonian as well as the corresponding coupling constants can be evaluated precisely by fitting the excitation frequencies obtained by THz spectroscopy [5,8,47], Raman spectroscopy [5,6,14,45], IR spectroscopy [31] and INS [4,30,44]. Thereby, the best fitting results for J and J' were found to be 4.38 meV and 0.15 meV, respectively [30,96]. A non-zero constant $\mathcal{K}$ will introduce cycloid deviation and splitting of the higher harmonics of the cycloid at every crossing of $\Phi_{\pm n}$ and $\Psi_{\pm n}$ in BFO [52].

However, avoidance of crossing and linear splitting in both the *ab* plane and *c* direction exist in the magnon spectrum at the zone boundary and were observed in single-crystal $YMnO_3$ INS measurements, shown in Fig. 3. Therefore, the following lattice term $\mathcal{H}_{\text{L}}$ and spin–lattice coupling term $\mathcal{H}_{\text{SL}}$ [43,73] need to be considered in the Hamiltonian [97,98]:

$$\mathcal{H}_{\text{L}} = \sum_{k,s} \omega_{k,s} a_{k,s}^{+} a_{k,s} \tag{12}$$

$$\mathcal{H}_{\text{SL}} = \sum_{i}\sum_{\alpha\beta\gamma\delta} G_{\alpha\beta\gamma\delta} S_i^{\alpha} S_i^{\beta} \epsilon_{\gamma\delta}^{i}, \tag{13}$$

where the bosonic operators $a_{k,s}$ with eigenenergies $\omega_{k,s}$ are for acoustic phonons in a hexagonal lattice in the absence of magnetic order in *h*-$YMnO_3$, and the spin–lattice coupling term $\mathcal{H}_{\text{SL}}$ is a hybridization term between the Holstein–Primakoff magnon operators S and G [43]. This term denote the elastic energy introduced by the configuration S^{α} and S^{β}, where G is the magnetoelastic coupling tensor and S is the spin–phonon coupling tensor, the summation index i extends over the spins of the whole crystal.

The phonon–magnon interaction was further studied by using a quasiharmonic free-energy approach implemented using first-principles methods, where the coupling was regarded as the dependence of the exchange constant on the atomic displacements [87], although the anharmonic effect was not fully considered. Using this method, researchers found that the cycloid in BFO has a third harmonic, which was supported by THz spectroscopy measurements [5,8,31].

Manipulation of quasiparticles

The strong interaction among the spin, polarization, and lattice in multiferroic materials provides plenty

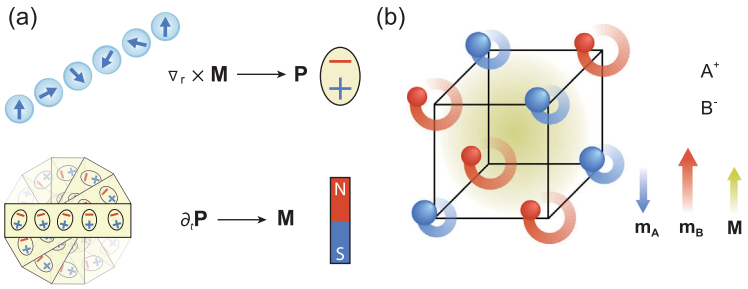

Figure 4. (a) Schematics of a polarization induced by a spatially varying magnetization and a magnetization induced by temporally varying polarization. (b) Magnetic moments from ionic loops. Perpendicular optical phonons drive ionic motion in a diatomic A^+B^- material. Local magnetic moments, $\mathbf{m_A}$ and $\mathbf{m_B}$, are created by the circular motions [100]. Copyright 2019, American Physical Society.

of space to manipulate the magnetization and polarization dynamically [99,100]. Previous researchers have put considerable effort into manipulating these features using strain [101–103]. In this article, an alternative method called 'dynamic multiferroics' will be reviewed. Magnetization M is symmetric under space inversion and antisymmetric under time reversal, whereas polarization P is symmetric under time reversal and antisymmetric under space inversion. Therefore, $M \sim P \times \partial P/\partial t$ can be developed in the presence of an appropriate dynamic polarization (Fig. 4).

This method supposes that $M \cdot (P \times \partial P/\partial t)$ couples M and P at the same order as $P \cdot (M \times (\nabla_r \times M))$. The time variation of P can be realized by considering two adjacent P evolving with different frequencies ω_1 and ω_2. In this case, two intrinsic lattice vibrations with these frequencies contribute to different Born effective charges. Four possible coupling mechanisms have been proposed: (1) phonon Zeeman splitting in a magnetic field, with perpendicular polarized phonons with frequencies $\omega_1 = \omega_2 = \omega_0$; (2) resonant magnon excitation by optically driven phonons with $\omega_1 \neq \omega_2$ with perpendicular polarity; (3) DM-type electromagnons, with an applied electric field and $P = (P_1(0),\ 0,\ P_2(t))$, where $P_1(0) = P_{\mathrm{FE}}(\omega_1 = 0, \varphi = \pi/2)$ and $P_2(t) = E(t)(\omega_2 = \omega_0)$, and (4) an inverse Faraday effect with perpendicular time-dependent polarizations induced by circularly polarized light both oscillating with the frequency of the light $(\omega_1 = \omega_2 = \omega_0)$ and phase-shifted by $\phi = \pi/2$. In multiferroic materials, each optical phonon is polarized with a certain polarization. Therefore, the above four schemes can be applied by carefully selecting activated phonons in a crystal.

Due to the recent development of THz technology, it is possible to activate phonons with frequencies in a certain range and certain polarizations. By combination with the strong coupling between the lattice and magnetic dynamics in multiferroic materials, it is thus possible to tune the magnetic states in these materials dynamically. The capabilities of this method were demonstrated by Fechner, as shown in Fig. 5 [104]. Fechner combined the well-established theory of non-linear phononics with spin dynamics, where the spin–lattice coupling was described through magnetic exchange interaction variations induced by structural changes and was demonstrated in three steps.

In the first step, the actual structural modification or atomic displacement induced via non-linear phononic coupling was evaluated by solving a set of dynamic equations, where an IR mode was excited by a driving sinusoidal force $F(t)$ with a certain amplitude and frequency:

$$\ddot{\xi}_{\mathrm{IR}} + \omega_{\mathrm{IR}}^2 \xi_{\mathrm{IR}} + \gamma_{\mathrm{IR}}\, \xi_{\mathrm{IR}}^3 = 2g\xi_{\mathrm{IR}}\xi_{\mathrm{R}} + F(t) \tag{14}$$

$$\ddot{\xi}_{\mathrm{R}} + \omega_{\mathrm{R}}^2 \xi_{\mathrm{R}} + \gamma_{\mathrm{R}}\, \xi_{\mathrm{R}}^3 = g\xi_{\mathrm{IR}}^2, \tag{15}$$

$$F(t) = E_{\mathrm{drive}} \sin(\omega t)\,, \tag{16}$$

where ξ_{R} and ξ_{IR} are the distortions of the Raman and IR modes, respectively; γ_{IR} and γ_{R} are the fourth-order anharmonic constants of the Raman and IR modes, respectively; and g is the coupling between two phonon modes. Depending on the non-linear coupling between different modes, several phonon components can be excited by the driving modes.

In the second step, after obtaining certain variations of the phonon modes, the lattice–spin interaction was included to consider the position deviation of the magnetic exchange interactions between spins

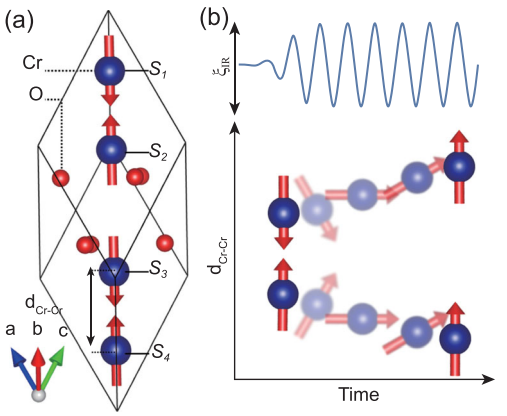

Figure 5. (a) Unit cell of Cr_2O_3. Red arrows represent the spin order. (b) Magnetic ground state changed by the excitation of a polar phonon mode [104]. Copyright 2019, American Physical Society.

i and j to first and second order as

$$H^{\mathrm{sp}} = \sum_{\langle i,j \rangle} \frac{\partial J_{i,j}}{\partial \xi}(\boldsymbol{S}_i \cdot \boldsymbol{S}_j)\xi + \sum_{i,j} \frac{\partial^2 J_{i,j}}{\partial \xi^2}(\boldsymbol{S}_i \cdot \boldsymbol{S}_j)\xi^2, \quad (17)$$

where the exchange interaction can be expressed as a function of the mode amplitude as

$$J_{i,j}(\xi_{\mathrm{R}}) = J_{i,j} + \frac{\partial J_{i,j}}{\partial \xi}\xi_{\mathrm{R}} + \frac{\partial^2 J_{i,j}}{\partial \xi^2}\xi_{\mathrm{R}}^2 + \cdots. \quad (18)$$

The last step was to consider the spin configuration evolution with respect to the time-dependent magnetic exchange modulations $J_{i,j}(\xi_{\mathrm{R}})$ and the usage of classical magnetization dynamics by applying the LLG equation, with an atomic approach:

$$\frac{dS_i}{dt} = -\frac{\gamma}{1+\alpha^2}\left[S_i \times H_i^{\mathrm{eff}}(t)\right] - \frac{\alpha\gamma}{1+\alpha^2}\left[S_i \times \left[S_i \times H_i^{\mathrm{eff}}(t)\right]\right], \quad (19)$$

where α is the damping parameter for spins. The magnetic energy $H_i^{\mathrm{eff}}(t)$ was evolved by using a Heisenberg Hamiltonian only considering $J_{i,j}$ and $D_{i,j}$.

In this way, the magnetic state was tuned from the equilibrium AFM of Cr_2O_3 to AFM ordering with ferromagnetically coupled NN spins. This transition is driven by the change in NN magnetic exchange interaction when the Cr–Cr separation is modified through non-linear coupling of the optical phonons to a symmetry-conserving A_{1g} Raman-active mode.

CONCLUSION

To achieve dynamic manipulation of magnetism as well as polarization, more detailed understanding of phonon–phonon and phonon–magnon interactions is required. Discrepancies still exist between the experimentally obtained dispersion curves and those theoretically predicted from first-principles or magnetic dynamics calculations. Moreover, demonstrations of the strong anharmonicity and illustrations of the ultrafast realistic evolution of these quasiparticles remain limited, either in terms of the resolution of the current characterization techniques or the capabilities of recent simulation methods. Despite these limitations, the strong coupling between phonons and magnons as well as electromagnons in AFM multiferroic materials makes it possible to apply the existing optical recording techniques for FMs to AFMs and to explore potential spintronic applications with ultrahigh speed and efficiency.

ACKNOWLEDGEMENTS

We gratefully acknowledge our colleagues and collaborators for sharing their insights and contributions, in particular, Drs J. M. Hu and L. Q. Chen.

FUNDING

This work was supported by the National Natural Science Foundation of China (51790494).

REFERENCES

1. Manipatruni S, Nikonov DE and Young IA. Beyond CMOS computing with spin and polarization. *Nat Phys* 2018; **14**: 338–43.
2. Němec P, Fiebig M and Kampfrath T *et al.* Antiferromagnetic opto-spintronics. *Nat Phys* 2018; **14**: 229–41.
3. Bloch F. Zur Theorie des Ferromagnetismus. *Z Phys* 1930; **61**: 206–19.
4. Park J-G, Le MD and Jeong J *et al.* Structure and spin dynamics of multiferroic $BiFeO_3$. *J Phys Condens Matter* 2014; **26**: 433202.
5. Talbayev D, Trugman SA and Lee S *et al.* Long-wavelength magnetic and magnetoelectric excitations in the ferroelectric antiferromagnet $BiFeO_3$. *Phys Rev B* 2011; **83**: 094403.
6. Cazayous M, Gallais Y and Sacuto A *et al.* Possible observation of cycloidal electromagnons in $BiFeO_3$. *Phys Rev Lett* 2008; **10**: 037601.
7. Toulouse C, Liu J and Gallais Y *et al.* Lattice and spin excitations in multiferroic h-$YMnO_3$. *Phys Rev B* 2014; **89**: 094415.
8. Skiadopoulou S, Goian V and Kadlec C *et al.* Spin and lattice excitations of a $BiFeO_3$ thin film and ceramics. *Phys Rev B* 2015; **91**: 174108.
9. Takahashi Y, Kida N and Yamasaki Y *et al.* Evidence for an electric-dipole active continuum band of spin excitations in multiferroic $TbMnO_3$. *Phys Rev Lett* 2008; **10**: 187201.
10. Haumont R, Kreisel J and Bouvier P *et al.* Phonon anomalies and the ferroelectric phase transition in multiferroic $BiFeO_3$. *Phys Rev B* 2006; **73**: 132101.
11. Fukumura H, Harima H and Kisoda K *et al.* Raman scattering study of multiferroic $BiFeO_3$ single crystal. *J Magn Magn Mater* 2007; **31**: E367–9.
12. Kothari D, Reddy VR and Sathe VG *et al* Raman scattering study of polycrystalline magnetoelectric $BiFeO_3$. *J Magn Magn Mater* 2008; **32**: 548–52.
13. Palai R, Schmid H and Scott JF *et al.* Raman spectroscopy of single-domain multiferroic $BiFeO_3$. *Phys Rev B* 2010; **81**: 064110.
14. Hlinka J, Pokorny J and Karimi S *et al.* Angular dispersion of oblique phonon modes in $BiFeO_3$ from micro-Raman scattering. *Phys Rev B* 2011; **83**: 020101.

15. Komandin GA, Torgashev VI and Volkov AA *et al.* Optical properties of $BiFeO_3$ ceramics in the frequency range 0.3-30.0 THz. *Phys Solid State* 2010; **52**: 734–43.
16. Kamba S, Nuzhnyy D and Savinov M *et al.* Infrared and terahertz studies of polar phonons and magnetodielectric effect in multiferroic $BiFeO_3$ ceramics. *Phys Rev B* 2007; **75**: 024403.
17. Lobo RPSM, Moreira RL and Lebeugle D *et al.* Infrared phonon dynamics of a multiferroic $BiFeO_3$ single crystal. *Phys Rev B* 2007; **76**: 172105.
18. Schleck R, Moreira R L and Sakata H *et al.* Infrared reflectivity of the phonon spectra in multiferroic $TbMnO_3$. *Phys Rev B* 2010; **82**: 144309.
19. Pailhès S, Fabrèges X and Régnault LP *et al.* Hybrid Goldstone modes in multiferroic $YMnO_3$ studied by polarized inelastic neutron scattering. *Phys Rev B* 2009; **79**: 134409.
20. Souchkov AB, Simpson JR and Quijada M *et al.* Exchange interaction effects on the optical properties of $LuMnO_3$. *Phys Rev Lett* 2003; **91**: 027203.
21. Fukumura H, Matsui S and Harima H *et al.* Raman scattering studies on multiferroic $YMnO_3$. *J Phys Condens Matter* 2007; **19**: 365239.
22. Zaghrioui M, Ta Phuoc V and Souza RA *et al.* Polarized reflectivity and lattice dynamics calculation of multiferroic $YMnO_3$. *Phys Rev B* 2008; **78**: 184305.
23. Vermette J, Jandl S and Mukhin AA *et al.* Raman study of the antiferromagnetic phase transitions in hexagonal $YMnO_3$ and $LuMnO_3$. *J Phys Condens Matter* 2010; **22**: 356002.
24. Beekman C, Reijnders AA and Oh YS *et al.* Raman study of the phonon symmetries in $BiFeO_3$ single crystals. *Phys Rev B* 2012; **86**: 020403.
25. Wang Y, Saal JE and Wu P *et al.* First-principles lattice dynamics and heat capacity of $BiFeO_3$. *Acta Mater* 2011; **59**: 4229–34.
26. Hermet P, Goffinet M and Kreisel J *et al.* Raman and infrared spectra of multiferroic bismuth ferrite from first principles. *Phys Rev B* 2007; **75**: 220102.
27. Wang DW, Weerasinghe J and Bellaiche L. Atomistic molecular dynamic simulations of multiferroics. *Phys Rev Lett* 2012; **10**: 067203.
28. Delaire O, Stone M B and Ma J *et al.* Anharmonic phonons and magnons in $BiFeO_3$. *Phys Rev B* 2012; **85**: 064405.
29. Schneeloch JA, Xu Z and Wen J *et al.* Neutron inelastic scattering measurements of low-energy phonons in the multiferroic $BiFeO_3$. *Phys Rev B* 2015; **91**: 064301.
30. Jeong J, Goremychkin EA and Guidi T *et al.* Spin wave measurements over the full Brillouin zone of multiferroic $BiFeO_3$. *Phys Rev Lett* 2012; **10**: 077202.
31. Kézsmárki I, Nagel U and Bordács S *et al.* Optical diode effect at spin-wave excitations of the room-temperature multiferroic $BiFeO_3$. *Phys Rev Lett* 2015; **11**: 127203.
32. Nagel U, Fishman RS and Katuwal T *et al.* Terahertz spectroscopy of spin waves in multiferroic $BiFeO_3$ in high magnetic fields. *Phys Rev Lett* 2013; **11**: 257201.
33. de Sousa R and Moore JE. Optical coupling to spin waves in the cycloidal multiferroic $BiFeO_3$. *Phys Rev B* 2008; **77**: 012406.
34. Katsura H, Balatsky AV and Nagaosa N. Dynamical magnetoelectric coupling in helical magnets. *Phys Rev Lett* 2007; **98**: 027203.
35. Senff D, Link P and Hradil K *et al.* Magnetic excitations in multiferroic $TbMnO_3$: evidence for a hybridized soft mode. *Phys Rev Lett* 2007; **98**: 37206.
36. Bowlan P, Trugman SA and Yarotski DA *et al.* Using ultrashort terahertz pulses to directly probe spin dynamics in insulating antiferromagnets. *J Phys D Appl Phys* 2018; **51**: 194003.
37. Takahashi Y, Shimano R and Kaneko Y *et al.* Magnetoelectric resonance with electromagnons in a perovskite helimagnet. *Nat Phys* 2011; **8**: 121–5.
38. Sushkov A B, Valdés Aguilar R and Park S *et al.* Electromagnons in multiferroic YMn_2O_5 and $TbMn_2O_5$. *Phys Rev Lett* 2007; **98**: 027202.
39. Pimenov A, Mukhin AA and Ivanov VY *et al.* Possible evidence for electromagnons in multiferroic manganites. *Nat Phys* 2006; **2**: 97–100.
40. Valdés Aguilar R, Sushkov AB and Zhang CL *et al.* Colossal magnon-phonon coupling in multiferroic $Eu_{0.75}Y_{0.25}MnO_3$. *Phys Rev B* 2007; **76**: 060404.
41. Oh J, Le MD and Nahm H-H *et al.* Spontaneous decays of magneto-elastic excitations in non-collinear antiferromagnet (Y,Lu)MnO_3. *Nat Commun* 2016; **7**: 13146.
42. Kadlec C, Goian V and Rushchanskii KZ *et al.* Terahertz and infrared spectroscopic evidence of phonon-paramagnon coupling in hexagonal piezomagnetic $YMnO_3$. *Phys Rev B* 2011; **84**: 174120.
43. Holm SL, Kreisel A and Schäffer TK *et al.* Magnetic ground state and magnon-phonon interaction in multiferroic h-$YMnO_3$. *Phys Rev B* 2018; **97**: 134304.
44. Jeong J, Le MD and Bourges P *et al.* Temperature-dependent interplay of Dzyaloshinskii-Moriya interaction and single-ion anisotropy in multiferroic $BiFeO_3$. *Phys Rev Lett* 2014; **11**: 107202.
45. Rovillain P, Cazayous M and Gallais Y *et al.* Polar phonons and spin excitations coupling in multiferroic $BiFeO_3$ crystals. *Phys Rev B* 2009; **79**: 180411.
46. Vermette J, Jandl S and Gospodinov MM. Raman study of spin-phonon coupling in $ErMnO_3$. *J Phys Condens Matter* 2008; **20**: 425219.
47. Matsubara E, Mochizuki T and Nagai M *et al.* Self-polarized terahertz magnon absorption in a single crystal of $BiFeO_3$. *Phys Rev B* 2016; **94**: 054426.
48. Krivoruchko VN. Electrically active magnetic excitations in antiferromagnets. *Low Temp Phys* 2012; **38**: 807–18.
49. Seki S, Kida N and Kumakura S *et al.* Electromagnons in the spin collinear state of a triangular lattice antiferromagnet. *Phys Rev Lett* 2010; **10**: 097207.
50. Lee J S, Kida N and Miyahara S *et al.* Systematics of electromagnons in the spiral spin-ordered states of *R*MnO_3. *Phys Rev B* 2009; **79**: 180403.
51. Takahashi Y, Yamasaki Y and Tokura Y. Terahertz magnetoelectric resonance enhanced by mutual coupling of electromagnons. *Phys Rev Lett* 2013; **11**: 037204.
52. Fishman RS, Furukawa N and Haraldsen JT *et al.* Identifying the spectroscopic modes of multiferroic $BiFeO_3$. *Phys Rev B* 2012; **86**: 220402.
53. Fishman RS. Field dependence of the spin state and spectroscopic modes of multiferroic $BiFeO_3$. *Phys Rev B* 2013; **87**: 224419.
54. Fishman RS, Haraldsen JT and Furukawa N *et al.* Spin state and spectroscopic modes of multiferroic $BiFeO_3$. *Phys Rev B* 2013; **87**: 134416.
55. Lee JH, Kezsmaki I and Fishman RS. First-principles approach to the dynamic magnetoelectric couplings for the non-reciprocal directional dichroism in $BiFeO_3$. *New J Phys* 2016; **18**: 043025.
56. Stenberg MPV and de Sousa R. Model for twin electromagnons and magnetically induced oscillatory polarization in multiferroic *R*MnO_3. *Phys Rev B* 2009; **80**: 094419.
57. Stenberg MPV and de Sousa R. Sinusoidal electromagnon in *R*MnO_3: indication of anomalous magnetoelectric coupling. *Phys Rev B* 2012; **85**: 104412.
58. Petit S, Moussa F and Hennion M *et al.* Spin phonon coupling in hexagonal multiferroic $YMnO_3$. *Phys Rev Lett* 2007; **99**: 266604.
59. Manz S, Matsubara M and Lottermoser T *et al.* Reversible optical switching of antiferromagnetism in $TbMnO_3$. *Nat Photon* 2016; **10**: 653–6.
60. Kanda N, Higuchi T and Shimizu H *et al.* The vectorial control of magnetization by light. *Nat Commun* 2011; **2**: 362.
61. Satoh T, Iida R and Higuchi T *et al.* Writing and reading of an arbitrary optical polarization state in an antiferromagnet. *Nat Photon* 2015; **9**: 25–9.
62. Dong S, Liu J-M and Cheong S-W *et al.* Multiferroic materials and magnetoelectric physics: symmetry, entanglement, excitation, and topology. *Adv Phys* 2015; **64**: 519–626.

63. Dzyaloshinsky I. A thermodynamic theory of 'weak' ferromagnetism of antiferromagnetics. *J Phys Chem Solids* 1958; **4**: 241–55.
64. Moriya T. Anisotropic superexchange interaction and weak ferromagnetism. *Phys Rev* 1960; **12**: 91–8.
65. Kimura T, Ishihara S and Shintani H *et al*. Distorted perovskite with e_g^1 configuration as a frustrated spin system. *Phys Rev B* 2003; **68**: 060403.
66. Dong S, Yu R and Yunoki S *et al*. Origin of multiferroic spiral spin order in the *R*MnO_3 perovskites. *Phys Rev B* 2008; **78**: 155121.
67. Yong-Mei T, Lin L and Shuai D *et al*. Multiferroic phase transitions in manganites *R*MnO_3: a two-orbital double exchange simulation. *Chin Phys B* 2012; **21**: 107502.
68. Furukawa N and Mochizuki M. Roles of bond alternation in magnetic phase diagram of *R*MnO_3. *J Phys Soc Jpn* 2010; **79**: 033708.
69. Fedorova NS, Ederer C and Spaldin NA *et al*. Biquadratic and ring exchange interactions in orthorhombic perovskite manganites. *Phys Rev B* 2015; **91**: 165122.
70. Fedorova NS, Windsor YW and Findler C *et al*. Relationship between crystal structure and multiferroic orders in orthorhombic perovskite manganites. *Phys Rev Mater* 2018; **2**: 104414.
71. Kaplan TA. Frustrated classical Heisenberg model in one dimension with nearest-neighbor biquadratic exchange: exact solution for the ground-state phase diagram. *Phys Rev B* 2009; **80**: 012407.
72. Solovyev I. Long-range magnetic interactions induced by the lattice distortions and the origin of the E-type antiferromagnetic phase in the undoped orthorhombic manganites. *J Phys Soc Jpn* 2009; **78**: 054710.
73. Mochizuki M, Furukawa N and Nagaosa N. Theory of spin-phonon coupling in multiferroic manganese perovskites *R*MnO_3. *Phys Rev B* 2011; **84**: 144409.
74. Fedorova NS, Bortis A and Findler C *et al*. Four-spin ring interaction as a source of unconventional magnetic orders in orthorhombic perovskite manganites. *Phys Rev B* 2018; **98**: 235113.
75. Ye F, Lorenz B and Huang Q *et al*. Incommensurate magnetic structure in the orthorhombic perovskite $ErMnO_3$. *Phys Rev B* 2007; **76**: 060402.
76. Lee N, Choi YJ and Ramazanoglu M *et al*. Mechanism of exchange striction of ferroelectricity in multiferroic orthorhombic $HoMnO_3$ single crystals. *Phys Rev B* 2011; **84**: 020101.
77. Kimura T, Goto T and Shintani H *et al*. Magnetic control of ferroelectric polarization. *Nature* 2003; **42**: 55–8.
78. Sergienko IA, Sen C and Dagotto E. Ferroelectricity in the magnetic E-phase of orthorhombic perovskites. *Phys Rev Lett* 2006; **97**: 227204.
79. Picozzi S, Yamauchi K and Sanyal B *et al*. Dual nature of improper ferroelectricity in a magnetoelectric multiferroic. *Phys Rev Lett* 2007; **99**: 227201.
80. Fennie CJ and Rabe KM. Magnetically induced phonon anisotropy in $ZnCr_2O_4$ from first principles. *Phys Rev Lett* 2006; **96**: 205505.
81. Xiang HJ, Kan EJ and Wei S-H *et al*. Predicting the spin-lattice order of frustrated systems from first principles. *Phys Rev B* 2011; **84**: 224429.
82. Novák P, Chaplygin I and Seifert G *et al*. Ab-initio calculation of exchange interactions in $YMnO_3$. *Comput Mater Sci* 2008; **44**: 79–81.
83. Alfe D. PHON: a program to calculate phonons using the small displacement method. *Comput Phys Commun* 2009; **18**: p. 2622–33.
84. Kunc K and Martin RM. Ab initio force constants of GaAs: a new approach to calculation of phonons and dielectric properties. *Phys Rev Lett* 1982; **48**: 406–9.
85. Graf M, Sepliarsky M and Tinte S *et al*. Phase transitions and antiferroelectricity in $BiFeO_3$ from atomic-level simulations. *Phys Rev B* 2014; **90**: 184108.
86. Iliev MN, Lee H-G and Popov VN *et al*. Raman- and infrared-active phonons in hexagonal $YMnO_3$: experiment and lattice-dynamical calculations. *Phys Rev B* 1997; **56**: 2488–94.
87. Cazorla C and Íñiguez J. Insights into the phase diagram of bismuth ferrite from quasiharmonic free-energy calculations. *Phys Rev B* 2013; **88**: 214430.
88. Togo A and Tanaka I. First principles phonon calculations in materials science. *Scripta Mater* 2015; **108**: 1–5.
89. Borissenko E, Goffinet M and Bosak A *et al*. Lattice dynamics of multiferroic $BiFeO_3$ studied by inelastic x-ray scattering. *J Phys Condens Matter* 2013; **25**: 102201.
90. Goffinet M, Hermet P and Bilc DI *et al*. Hybrid functional study of prototypical multiferroic bismuth ferrite. *Phys Rev B* 2009; **79**: 014403.
91. Singh MK, Ryu S and Jang HM. Polarized Raman scattering of multiferroic $BiFeO_3$ thin films with pseudo-tetragonal symmetry. *Phys Rev B* 2005; **72**: 132101.
92. Singh MK, Jang HM and Ryu S *et al*. Polarized Raman scattering of multiferroic $BiFeO_3$ epitaxial films with rhombohedral R3c symmetry. *Appl Phys Lett* 2006; **88**: 042907.
93. Rushchanskii KZ and Lezaic M. Ab initio phonon structure of h-$YMnO_3$ in low-symmetry ferroelectric phase. *Ferroelectrics* 2012; **426**: 90–6.
94. Sim H, Oh J and Jeong J *et al*. Hexagonal *R*MnO_3: a model system for two-dimensional triangular lattice antiferromagnets. *Acta Crystallogr B Struct Sci Cryst Eng Mater* 2016; **72**: 3–19.
95. Holstein T and Primakoff H. Field dependence of the intrinsic domain magnetization of a ferromagnet. *Phys Rev* 1940; **58**: 1098–113.
96. Matsuda M, Fishman RS and Hong T *et al*. magnetic dispersion and anisotropy in multiferroic $BiFeO_3$. *Phys Rev Lett* 2012; **10**: 067205.
97. Boiteux M, Doussineau P and Ferry B *et al*. Antiferroacoustic resonances and magnetoelastic coupling in $GdAlO_3$. *Phys Rev B* 1972; **6**: 2752–62.
98. Laurence G and Petitgrand D. Thermal conductivity and magnon-phonon resonant interaction in antiferromagnetic $FeCl_2$. *Phys Rev B* 1973; **8**: 2130–8.
99. Juraschek DM, Fechner M and Spaldin NA. Ultrafast structure switching through nonlinear phononics. *Phys Rev Lett* 2017; **11**: 054101.
100. Juraschek DM, Fechner M and Balatsky AV *et al*. Dynamical multiferroicity. *Phys Rev Mater* 2017; **1**: 014401.
101. Nan C-W, Bichurin MI and Dong S *et al*. Multiferroic magnetoelectric composites: historical perspective, status, and future directions. *J Appl Phys* 2008; **10**: 031101.
102. Hu J-M, Duan C-G and Nan C-W *et al*. Understanding and designing magnetoelectric heterostructures guided by computation: progresses, remaining questions, and perspectives. *npj Comput Mater* 2017; **3**: 18.
103. Zhu M, Nan T and Peng B *et al*. Advances in magnetics epitaxial multiferroic heterostructures and applications. *IEEE Trans Magn* 2017; **53**: 1–16.
104. Fechner M, Sukhov A and Chotorlishvili L *et al*. Magnetophononics: ultrafast spin control through the lattice. *Phys Rev Mater* 2018; **2**: 064401.